2024 IEEE/RSJ International Conference on Intelligent Robots and Systems (IROS)
October 14-18, 2024. Abu Dhabi, UAE

Intraocular Reflection Modeling and Avoidance Planning in Image-Guided Ophthalmic Surgeries

Junjie Yang[1], Zhihao Zhao[1], Yinzheng Zhao[2], Daniel Zapp[2], Mathias Maier[2], Kai Huang[3], Nassir Navab[1], *Fellow, IEEE*, M. Ali Nasseri[2]

***Abstract*— Intuitive enhancement of surgical precision in robotic retinal surgery highly depends on the stable acquisition of intraocular imaging data. Such acquisition requires segmenting intraocular components, especially instrument-tip positions, to achieve state estimation and subsequent navigation and motion control. However, intraocular light reflections and glares significantly impact instrument segmentation, state estimation, and subsequent visual servoing in retinal surgery. At the same time, light reflections are among the sources of information for intraoperative navigation. In this work, we propose a method for modeling and optimizing light reflections using microscopy as the standard surgical imaging modality. Beyond optimization, our approach seamlessly integrates the optimized reflection with path planning, strategically circumventing reflection areas and ensuring uninterrupted visibility of instrument tips throughout the surgical procedure. Experiments demonstrate the methodology's efficacy in avoiding glare affections during eye surgeries.**

I. Introduction

In ophthalmic surgeries, surgeons monitor the instruments' status through the microscope and decide the subsequent motion control. Specifically, the retinal surface, the light probe, the instrument, and its shadow are essential for deciding the next step of surgical manipulation. However, intense glares are caused by intraocular reflection, sporadically preventing the surgeon from acquiring the instrument's position in the microscope image. On the one hand, the surgeon may suffer from visual blockage due to the instant strong reflection and must pause the surgery until the sense of sight recovers. On the other hand, the intraocular reflection either blocks the projection of above-retinal instrument tips or interferes with the shaping of intra-retinal instrument shadows, which affects the status monitoring of instruments and turns off the subsequent motion control, as shown in Fig. 1. This problem occurs explicitly during the fluid-air exchange in vitrectomy surgeries [1]–[3]. Therefore, the intraocular reflection should be relieved to ensure the visibility of necessary image components during eye surgeries.

Since the light probe is needed in eye surgeries to provide intraocular illumination, intraocular reflections are classified into three types depending on the object's surface of reflection: retinal reflection, vitreous reflection, and instrument reflection. Retinal reflection occurs if a particular retinal area suffers from diseases that cause rough tissue deformation. Vitreous reflection happens when the vitreous liquid is partially extracted from the irrigation device, shaping an intersection plane between the vitreous liquid and the intraocular air, which causes light reflection and refraction to shape glares. Instrument reflection occurs when the light probe is placed toward the metal instrument, leading to a strong reflection on the instrument's metal surface that causes the bothering glare shock but also contributes to the pose estimation in some scenarios.

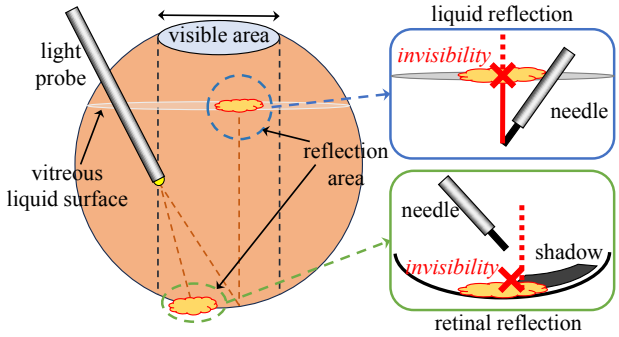

Fig. 1: Affection of intraocular glares in eye surgeries.

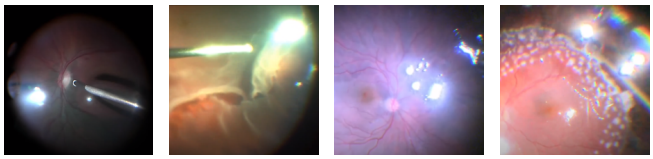

(a) ERMs peeling [4]. (b) Retina detachment [5]. (c) Retina detachment [6]. (d) Retina detachment [7].

Fig. 2: Examples of intraocular reflections and glares affecting instrument monitoring in different eye surgeries.

Currently, many methods propose physical devices [8]–[11] to relieve the affection of reflections and glares while capturing static retina images for preoperative diagnosis. However, this requires additional installation and validation in the operating room for intraoperative purposes. Many papers also focus on the intraoperative manipulation of light probes to navigate the instrument's motion [12]–[18]. However, few papers [19] consider the intraocular reflections, not to mention the subsequent visual blockage. Once the light reflection appears on the predefined instrument trajectory, these microscope-guided methods fail to continue generating manipulation commands for both human surgeons and robots. Although some works [20], [21] use neural network

[1]Technical University of Munich, 80333 Munich, Germany {junjie.yang,zhihao.zhao,nassir.navab}@tum.de
[2]Klinikum rechts der Isar, 81675 Munich, Germany {daniel.zapp,mathias.maier}@mri.tum.de, ali.nasseri@tum.de, yinzheng.pro@gmail.com
[3]Sun Yat-Sen University, 510006 Guangzhou, China huangk36@mail.sysu.edu.cn

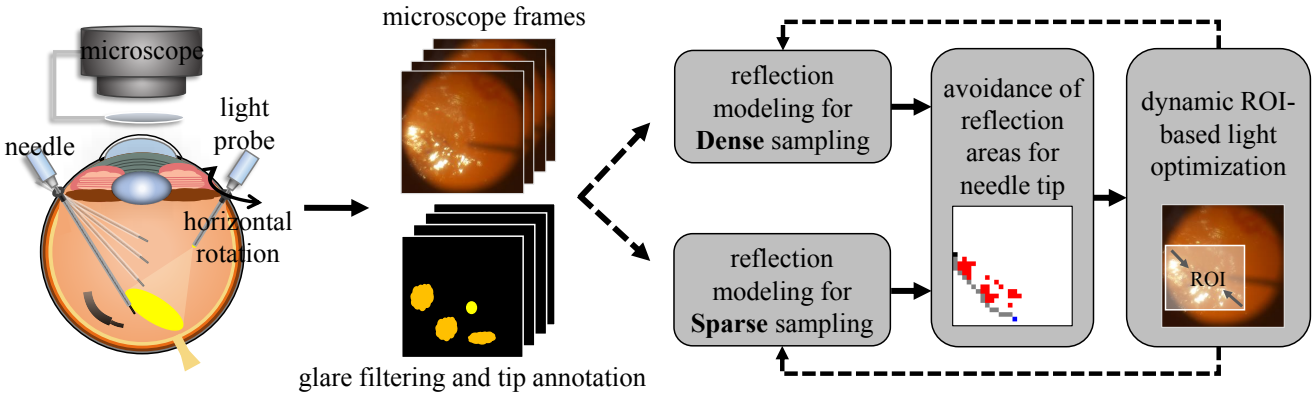

Fig. 3: Overview of our method on an eye phantom including reflection extraction, modeling and avoidance .

to remove glares in the image by denoising and inpainting, their performance of recovering shadow information within the glare areas are still questioned.

Considering the retinal and vitreous reflections unified as visual blockage, this paper proposes adjusting the light probe's orientation to model the reflection distribution and generate a locally optimal reflection. By rasterizing the retina in the microscope, the collected microscope frames along the light probe's rotation form a reflection map to approximate how the light reflection is distributed in each rasterized retinal cell. This reflection map is then used to find the global minimal reflection and the corresponding position of the light-probe tip. Then, based on the optimized reflection distribution, we use the A-star algorithm to plan a path for the instrument tip from its current position to the target retinal area in the microscope scope without stepping into the reflection areas, avoiding the failure of finding image components for decision-making.

The contributions of this paper are listed below:

- The intraocular reflection is modeled and optimized using sampled microscope frames.
- The reflection avoidance is achieved by combining reflection modeling and path planning.
- A dynamic ROI-based light optimization method is proposed to further improve the visibility of instruments during their intraocular movement.

II. Method

The overview of our method is presented in Fig. 3. This paper uses the instrument as a needle to cover common surgical scenarios. Since the frame sampling in Fig. 3 can be conducted before all surgical manipulations, its computational cost needs additional analysis in the future.

A. Construction of Reflection Map

Assume that the region of interest (ROI) of the retina in the microscope is bounded as a square area shaped as $dim \times dim$ pixels. The microscope image's color space is already converted from RGB to grayscale. Given a predefined granularity σ_{ras} pixels for image rasterization, each dimension of the retina area is divided into $s_{img} = \text{ceil}(dim/\sigma_{ras})$ cells, while σ_{ras} can be adjusted according to the granularity level of modeling the reflection.

We use $C_{i,j}, i, j \in [0, s_{img} - 1]$ to denote the retinal cell in the j-th column of the i-th row. Then, the reflection distribution in this cell $C_{i,j}$ is represented by its reflection score, which is the sum of normalized reflection strength after non-reflection pixels are filtered as equation (1).

$$\begin{aligned} \forall p \in C_{i,j}, S_{i,j} &= \sum \frac{\text{filter}(p, \sigma_{sr})}{255}, \\ \text{filter}(p, \sigma_{sr}) &= \begin{cases} p, & \text{if } p >= \sigma_{sr} \\ 0, & \text{if } p < \sigma_{sr} \end{cases} \end{aligned} \tag{1}$$

where p is the pixel value and σ_{sr} is a hyper-parameter threshold to define whether a pixel belongs to strong light reflection. The cell containing the light-probe tip in the image will be ignored for the reflection score's calculation.

The reflection score $S_{i,j}$ of each cell $C_{i,j}$ only represents the reflection distribution from the current light direction from the current light-probe tip in the image. Therefore, we horizontally rotate the light probe (initial orientation θ_{ltip}) by $\Delta\theta_{ltip}$ degrees and sample m continuous frames during the light probe's one-direction rotation to generate the reflection distribution. Then, we mark the relative angle from the current light-probe tip to the cell center as $\theta^k_{i,j}$ where $k \in [0, m-1]$ indicates the k-th frame in the collected frames. If the light-probe tip p_{ltip} is visible in the microscope image, the relative light-cell angle $\theta^k_{i,j}$ can be calculated as equation (2).

$$\theta^k_{i,j} = \frac{\vec{v}_x \cdot \vec{v}_{cc \to ltip}}{\|\vec{v}_x\| \|\vec{v}_{cc \to ltip}\|} \cdot \text{sign}(\vec{v}_x \times \vec{v}_{cc \to ltip}), \tag{2}$$

where $\vec{v}_x$ is the global x-axis (column axis) vector and $\vec{v}_{cc \to ltip}$ is the vector from the center of the (i, j)-th cell to the light-probe tip. Function $\text{sign}(val)$ returns the sign of a given value val. If the light tip p_{ltip} is not visible in the tip, the relative angle $\theta^k_{i,j}$ can be used only as a position marker.

Temporarily, we combine all m reflection maps into a global reflection map with the same size. Then, each cell $C^{global}_{i,j}$ in the global map contains a sequence of tuples $< \theta^k_{i,j}, S^k_{i,j} >, k \in [0, m-1]$, and the reflection modeling task is to integrate all reflection scores into a global distribution. In

this paper, we propose two strategies to generate the global distribution.

B. Reflection Modeling from Sparse Sampling

If the light-probe tip is visible in the frame, sparse frame sampling is needed to collect frames for the reflection approximation. Based on the assumption that the reflection of a local retinal area varies continuously, the reflection distribution in the cell $C_{i,j}^{global}$ is approximated by the interpolation of reflection strengths in sampled frames, as shown in Fig. 4. Using the reflection sequence $< \theta_{i,j}^{k}, S_{i,j}^{k} >$

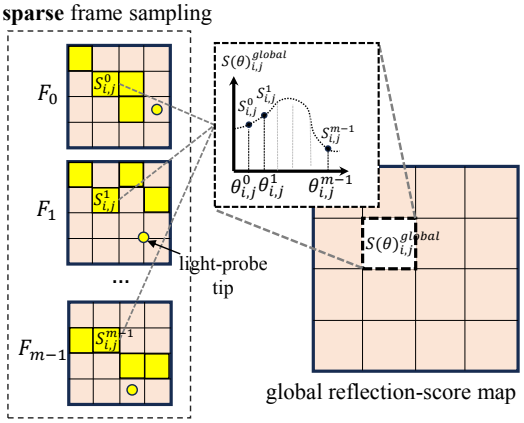

Fig. 4: Sparse modeling by polynomial interpolation.

$, k \in [0, m-1]$ as the sampled X-Y values in a planar function, then this reflection function can be approximated by polynomial interpolation as equation (3).

$$S(\theta)_{i,j}^{global} = |\sum_{k=0}^{m-1}(\prod_{0 \leqslant l \leqslant m-1}^{k \neq l} \frac{\theta - \theta_{i,j}^{l}}{\theta_{i,j}^{k} - \theta_{i,j}^{l}})\ S_{i,j}^{k}| \tag{3}$$

After obtaining the interpolated reflection-score distribution function $S(\theta)_{i,j}^{global}$ of the global cell $C_{i,j}^{global}$, the global reflection optimization can be achieved by finding the ideal light-probe tip p_{ltip} during its horizontal rotation so that the sum of reflection strengths in all global reflection cells reach the minimal value with corresponding relative light-cell angles. This problem is formalized as equation (4).

$$\arg\min_{p_{ltip}} \sum_{i=0,j=0}^{s_{img}-1} S(\theta_{i,j})_{i,j}^{global} \tag{4}$$

where the calculation of relative angle $\theta_{i,j}$ from each cell center to the given light-probe tip p_{ltip} is done as equation (2). The corresponding light-probe tip becomes optimal if the minimal reflection score is found.

However, it is still difficult to consider all reflection cells for global optimization due to the computational cost. Therefore, the solution to finding the optimal among the continuous reflection distribution can be approximated by finding the discrete frame with the optimal reflection. It means we can horizontally rotate the light-probe to generate a discrete sequence of light-probe tips and search for the optimal reflection frame in the sequence. Defining a range of rotation angles $[\theta_{ltip}^{min}, \theta_{ltip}^{max}]$ and an angle granularity $\Delta\theta_{rot}$, we can define a sequence of light-probe tip positions $\mathcal{T}_{ltip}$, as equation (5).

$$\mathcal{T}_{ltip} = \{p_i = \theta_{ltip}^{min} + \Delta\theta_{rot} \cdot i | \theta_{ltip}^{min} \leqslant p_i \leqslant \theta_{ltip}^{max}, i \in \mathbb{N}\} \tag{5}$$

Then, giving each static light-probe placement $p_{ltip} \in \mathcal{T}_{ltip}$, the reflection strength in each cell can be calculated using equations (2) and (3) together. Consequently, the whole reflection score in the corresponding frame is obtained by adding all cells' reflections. During the light probe's horizontal rotation, the light probe's intraocular radius (the length of the light probe's intraocular portion) remains unchanged, obeying the RCM constraint of trocar placement. Finally, the solution to problem (4) is approximated as equation (6).

$$\arg\min_{p_i \in \mathcal{T}_{ltip}} \sum_{i=0,j=0}^{s_{img}-1} S_{i,j}(\theta_{ltip}(p_i)) \tag{6}$$

C. Reflection Modeling from Dense Sampling

A dense frame sampling can approximate the reflection distribution if the perception and calculation system can work at a high frequency. In this context, the sum of reflection strength within the map serves as a representative reflection score when the light probe remains in a fixed position. We collect the annotated light-tip position l^i as well as the reflection score S^i of each sampled frame to build a global look-up table, as shown in Fig. 5. This reflection score S^i can be either the sum of reflection for global optimization or the collection of all reflection cells in the frame for dynamic optimization. Traversing all items in the global look-up table makes it straightforward to find the frame with the minimal reflection score. Subsequently, the corresponding light-tip position of the minimal-score frame is recovered to duplicate the same reflection distribution. This method guides surgeons and robotic systems to position the light probe optimally, thereby reducing reflection challenges and enhancing surgical precision in cases that demand dense frame maps, as shown in Fig. 5.

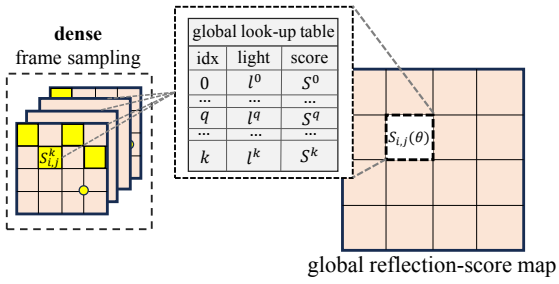

Fig. 5: Dense reflection modeling by a global look-up table.

If the collected frames are dense enough, it is intuitive to find the frame in the frame collection with the minimal global reflection scores as the target reflection status using equation (7).

$$\arg\min_{k \in [0,m-1]} \sum_{i=0,j=0}^{s_{img}-1} S_{i,j}^{k} \tag{7}$$

III. Reflection Avoidance

Upon obtaining the optimal reflection map, the light probe should be placed at the corresponding optimal position with a suppressed reflection distribution. However, avoiding image cells where strong reflections still exist is essential. Therefore, the next step is leveraging the optimal reflection map to generate a future needle-tip trajectory to avoid collisions between the needle tip and the remaining reflection areas. Also, this planned trajectory is fundamental to ensuring the precision and safety of ophthalmic surgery.

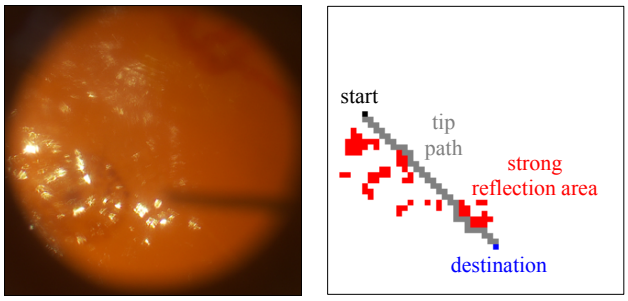

(a) Input frame. (b) Output path.

Fig. 6: An examples of reflection-based path planning for a given frame using the 8-neighbor searching strategy.

Given that areas of strong reflection have been rasterized into cells within the optimal reflection map, the objective is to generate a path from the current needle tip to the target area. Importantly, every cell traversed along this path should be a non-reflection cell. A classical Astar algorithm is adopted to achieve this intricate path-planning task. The Astar algorithm is renowned for finding the shortest path while considering obstacles and constraints, making it an ideal choice for guiding the needle tip safely through the intricate landscape of reflection and retinal surfaces. We adopt the general evaluation function as equation (8) to assess the rank of each cell during path planning.

$$\begin{aligned} forward(x) &= dis(C, C_{ending}) \\ g(C) &= history(C) * 1.0 + forward(C) * 1.0 \end{aligned} \tag{8}$$

Suppose no valid path is obtained during the path planning stage. In this case, human intervention is needed to raise the threshold of glare filtering to enable more traversable cells, which sacrifices the tolerance of reflection perception and requires higher-precision instrument manipulation.

IV. Dynamic ROI-based Light Optimization

Initially, the reflection of the microscope frame is modeled by dense or sparse sampling, and the trajectory of the needle tip p_{ntip} is planned. However, the surgeon mainly focuses on the Region of Interest (ROI) surgical area and dynamically adjusts the needle-tip position. In this paper, we define the surgical ROI as the rectangle area in the reflection map bounded by the target needle-tip position p_{tar} and the current needle-tip position p_{cur} as corners of the rectangle, as (9). This rectangle ROI is represented by its left-up corner, width, and height.

$$\begin{aligned} \text{Width}_{ROI} &= \|p_{tar}.x - p_{cur}.x\| \\ \text{Height}_{ROI} &= \|p_{tar}.y - p_{cur}.y\| \\ p_{leftup} &= (\min(p_{tar}.x, p_{cur}.x), \min(p_{tar}.y, p_{cur}.y)) \end{aligned} \tag{9}$$

Once a valid path T_{ntip} is planned from the current needle tip to the target position without reaching, the following algorithm can adjust the light and optimize the reflection strength in the ROI.

Algorithm 1 Dynamic ROI-based Light Optimization

while $p_{cur} \neq p_{tar}$ **do**
  $C^k = \arg\min_{k \in [0, m-1]} \sum_{i,j} S^k_{i,j}$(ROI)
  $T_{ntip} = \text{PathPlanning}(p_{cur}, p_{tar})$
  AdjustLightPlacement(C^k)
  $p_{next} = T_{ntip}[1]$
  MoveNeedle(p_{cur},p_{next}) *# conduct needle movement*
  $p_{cur} = p_{next}$ *# update needle status after movement*
  ROI = UpdateROI(p_{cur}, p_{tar})
end while

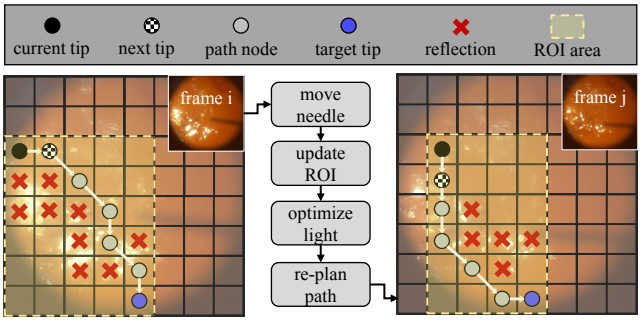

Fig. 7: Dynamic light optimization and reflection avoidance based on the reflection inside the ROI.

As presented in **Algorithm 1**, in each loop of motion control, the best reflection map with the lowest reflection score in the ROI area is found and used to generate a new path from the current needle tip p_{cur} towards the target p_{tar}. Function MoveNeedle(p_{cur},p_{next}) represents the actuating procedure of moving the instrument tip from the current position p_{cur} to the next target node p_{next}, which can be solved as an ophthalmic path-tracking problem (similar to vessel tracking [22]). Subsequently, the new ROI of motion control is updated according to the needle tip's current position p_{cur} and destination p_{tar}. This procedure is also depicted in Fig. 7.

This dynamic ROI-based reflection modeling adjusts the light probe with the needle-tip motion. We can follow this algorithm to ensure that the ROI's reflection is optimized to help surgeons better observe the manipulation area and avoid losing the needle-tip position due to glares. It is noticeable that the reflection strength in the ROI area is optimized to provide a higher possibility of planning a path in the ROI.

However, the input of the path-planning module is still the whole reflection map to ensure the connectivity between the current needle tip and the target tip position.

V. Experiment and Result

A. Design of Experiment

We collect 21 frames of the phantom retina reflection, as shown in Fig. 8. These frames are used for the evaluation of

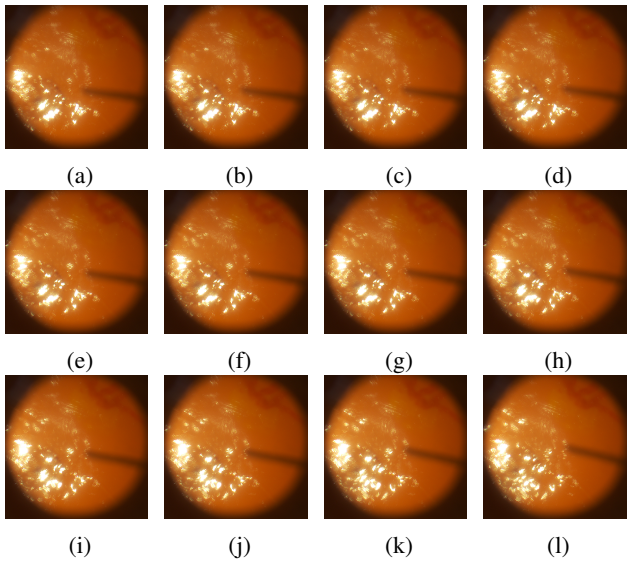

Fig. 8: 12 examples out of 21 frames by clockwise and horizontally rotating the light probe in a eye phantom for experiments (12mm-diameter visible range).

retinal reflection modeling using the following steps:

- Rasterize all frames ($dim = 1040$ pixels) into cells ($\sigma_{ras} = 40$ pixels) and calculate their reflection scores using equation (1). The reflection threshold σ_{sr} is 220 for each pixel.
- Sample frames from the collection depending on the sampling interval (number of continuous frames to sample one output), $[1, 2, 4, 6, 8, 10]$ for the dense sampling and $[4, 6, 8, 10]$ for the sparse sampling ($[1, 2]$ ignore for the sparse sampling due to the sparse feature). For each sampling interval, 10 random samplings are conducted to generate a collection of microscope frames for reflection modeling and path planning.
- Use the dense and sparse sampling strategies to approximate the reflection distribution and find the minimal reflection frame with the lowest reflection score. A light-tip sequence is generated by rotating the light probe from the starting frame to the ending frame, simplifying the calculation for sparse sampling.
- After obtaining the minimal reflection frame, use the A-star planning to generate a path from the starting cell $[4, 3]$ to the ending cell $[25, 12]$ to avoid reflection cells.

To evaluate the performance of two different reflection-modeling strategies, we use the following metrics:

- relative reflection strength: the ratio of the found minimal reflection score over the global minimal reflection score (indicating how approximating the found frame is to the global optimal frame). The global minimal reflection score is ≈ 22106.17 as a prior.
- relative path length: the ratio of the planned path with reflection avoidance in the found minimal reflection frame over the straight path length from the starting cell's pixel center to the ending cell's pixel center (913.89 pixels).
- number of avoided strong-reflection cells: proving the necessity of reflection avoidance.

During the approximation of sparse modeling, the angle granularity $\Delta\theta_{rot}$ is $1°$, and the rotation range is $[161°, 172°]$ referring to the x-axis (the column axis of the input image).

B. Result of Reflection Modeling

The distribution of relative reflection strengths in different sampling intervals is presented in Fig. 9. As for the dense sampling strategy, the approximation of reflection strength is enhanced when the sampling interval is reduced, making it easier to sample frames with reflection strengths similar to those of the global minimal frame. However, the sparse sampling method obtains the best approximation result (mean) when the sampling interval is 8. Its performance worsens when the sampling interval length decreases due to the unstable approximation by polynomial interpolation. This phenomenon is caused by the substantial and unstable strength variation between two samples if the sampling interval is too small during interpolation, which shows its feasibility only in the sparse-sampling scenario.

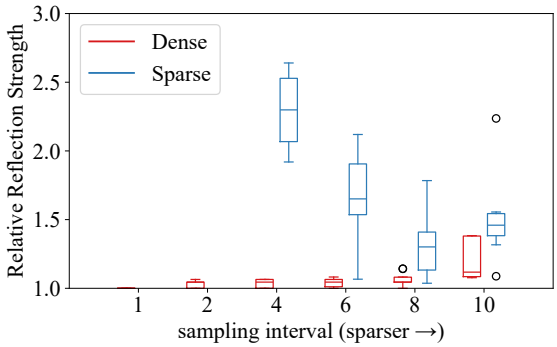

Fig. 9: Comparison of relative reflection strength using dense and sparse sampling strategies, respectively.

The length distribution of planned paths by Astar is presented in Fig. 10. Since the dense sampling method can find the low-reflection frame closer to that of the global minimal frame, the number of strong-reflection cells is reduced. Consequently, the path planner can generate a short path for the dense sampling method compared with the sparse sampling.

We also count the number of strong reflection cells that are avoided by reflection optimization and path planning compared with the straight path from the starting cell to the ending cell, as shown in TABLE I, which proves the necessity of avoiding reflection areas to ensure the visibility of surgical instruments.

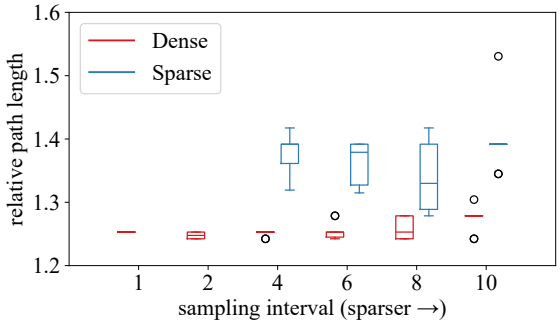

Fig. 10: Comparison of relative path length using dense and sparse sampling strategies.

TABLE I: Number of avoided reflection cells

sampling interval	method	mean	variance	min	max
10	dense	13.6	0.64	12	14
	sparse	14.5	0.45	13	15
8	dense	10.4	9.84	6	14
	sparse	14.6	0.24	14	15
6	dense	8.7	8.41	6	14
	sparse	15.0	0.0	15	15
4	dense	7.0	1.2	6	9
	sparse	15.0	0.0	15	15
2	dense	7.6	2.04	6	9
	sparse	-	-	-	-
1	dense	6.0	0.0	6	6
	sparse	-	-	-	-

The experiment results show that the sparse-sampling method obtains a relatively stable number of avoided reflection cells with its best performance at sampling interval 8. By contrast, the dense sampling method can improve the reflection-avoidance performance with the decreasing sampling interval. Meanwhile, sampling methods and the path-planning module can prevent human surgeons and robotic perception systems from stepping into strong-reflection areas.

C. Testing Dynamic ROI Optimization

We collect the average reflection strengths (sum of ROI strengths/number of path nodes) in the ROI of three light-placement optimization methods with multiple sampling interval sizes [1:1:10]. To compare the improvement of the dynamic ROI-based optimization, we use the average ROI strengths along the planned path in each simulation, as shown in (10), to demonstrate the reflection strength along the planned path. For each sampling interval, 50 simulations are conducted, and their average ROI strengths are adopted for the method comparison.

$$\begin{aligned} ROI^i &= \text{UpdateROI}(p^i_{cur}, p_{tar}),\ p^i_{cur} \in T_{ntip} \\ Sum &= \sum S^i(ROI^i) \\ metric &= Sum\ /\ (\text{NumOfNode}(T_{ntip}) - 1) \end{aligned} \tag{10}$$

This test uses the dense-sampling strategy to model the reflection strength with the global-min(imal) frame as the ground truth. In this experiment, the initial and target needle-tip positions in the rasterized reflection map are $[0, 10]$ and $[13, 24]$, respectively. We allow traversing the eight neighborhood nodes in the reflection map for Astar path planning. The result is depicted in Fig. 11.

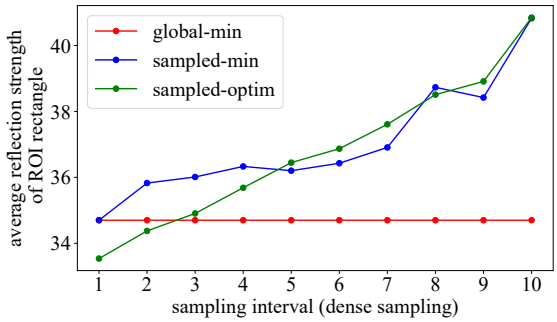

Fig. 11: Comparison of average ROI strength along planned paths using different sampling strategies and intervals.

According to the trend of average ROI strengths, if the frames for the light-probe placement are densely sampled (i.e., interval size as 1 and 2), the dynamic sampled-optimization strategy helps to obtain reduced ROI reflection strengths even better than using the global-minimal frame. As for the interval sizes 3 and 4, although the ROI strengths of the sampled-minimal method are higher than the ground truth, it still surpasses the result of using the fixed sampled-minimal frame for path planning. However, when the sampling interval is too sparse ([5:1:10]), the strength variations of sampled-min and sampled-optimal methods are similar. The result shows the weakness of losing reflection information due to sparse sampling, proving that relatively dense frame sampling benefits the dynamic ROI-based light optimization.

VI. Conclusion

This paper tries to improve the instrument tip's trajectory planning under the challenge of glare-caused intraocular invisibility. The proposed method considers a simple scenario of static reflection distribution that can be modeled during the surgical preparation stage. Then, this paper proposes adjusting the light probe's placement to obtain suppressed reflection. It provides a dynamic ROI-based light optimization during the needle movement, relieving the visual interruption of strong reflections instrument manipulation.

Meanwhile, using irrigation devices in the surgical setup maintains the intraocular pressure balance but leads to a varying fluid environment inside the eyeball and causes unpredictable illumination results. Moreover, unstable eyeball-microscope alignment due to the eyeball's orbital control also slightly changes the angles of light refraction and generates more reflection areas. Therefore, the proposed reflection modeling and avoidance need additional validation to meet the higher surgical safety in real eye surgeries with more complicated illumination conditions.

REFERENCES

[1] Y.-H. Cheng, H. Wang, B. Li, M. Ji, Q. Shi, Y. Qi, Y.-G. Hu, A.-M. Xie, and C. Pei, "Vitrectomy with air tamponade for surgical repair of rhegmatogenous retinal detachment by eye position guided fluid-air exchange," *Int. J. Ophthalmol.*, vol. 13, no. 9, pp. 1417–1422, Sept. 2020.

[2] D. H. Nam, M. Ku, H. J. Sohn, and D. Y. Lee, "Minimal fluid-air exchange in combined 23-gauge sutureless vitrectomy, phacoemulsification, and intraocular lens implantation," *Retina*, vol. 30, no. 1, pp. 125–130, Jan. 2010.

[3] Q. Wang, J. Zhao, Q. Xu, C. Han, B. Hou, and Y. Huang, "Visual outcomes and complications following one-way air-fluid exchange technique for vitreous hemorrhage post vitrectomy in proliferative diabetic retinopathy patients," *BMC Ophthalmol.*, vol. 21, no. 1, p. 129, Mar. 2021.

[4] W. E. Hospital, "Epiretinal membrane peel," 2019. [Online]. Available: https://www.youtube.com/watch?v=azZPOImW_4s&ab_channel=WillsEyeHospital

[5] Cybersight, "Lecture: Retinal detachment," 2021. [Online]. Available: https://www.youtube.com/watch?v=TdUYC7rQY_I&ab_channel=Cybersight

[6] ——, "Surgery: Vitrectomy for retinal detachment: Assortment of cases," 2021. [Online]. Available: https://www.youtube.com/watch?v=Kw719M6tfQY&t=309s&ab_channel=Cybersight

[7] ——, "Surgery: Complex retinal detachment with pvr," 2021. [Online]. Available: https://www.youtube.com/watch?v=wXrvI2WWlyM&ab_channel=Cybersight

[8] A. Rossi, M. Rahimi, T. Son, R. V. P. Chan, M. J. Heiferman, and X. Yao, "Preserving polarization maintaining photons for enhanced contrast imaging of the retina," *Biomed. Opt. Express*, vol. 14, no. 11, pp. 5932–5945, Nov 2023. [Online]. Available: https://opg.optica.org/boe/abstract.cfm?URI=boe-14-11-5932

[9] M. Damodaran, K. V. Vienola, B. Braaf, K. A. Vermeer, and J. F. de Boer, "Digital micromirror device based ophthalmoscope with concentric circle scanning," *Biomed. Opt. Express*, vol. 8, no. 5, pp. 2766–2780, May 2017. [Online]. Available: https://opg.optica.org/boe/abstract.cfm?URI=boe-8-5-2766

[10] D. W. Palmer, T. Coppin, K. Rana, D. G. Dansereau, M. Suheimat, M. Maynard, D. A. Atchison, J. Roberts, R. Crawford, and A. Jaiprakash, "Glare-free retinal imaging using a portable light field fundus camera," *Biomed. Opt. Express*, vol. 9, no. 7, pp. 3178–3192, Jul 2018. [Online]. Available: https://opg.optica.org/boe/abstract.cfm?URI=boe-9-7-3178

[11] K. Guo, Z. Bian, S. Dong, P. Nanda, Y. M. Wang, and G. Zheng, "Microscopy illumination engineering using a low-cost liquid crystal display," *Biomed. Opt. Express*, vol. 6, no. 2, pp. 574–579, Feb 2015. [Online]. Available: https://opg.optica.org/boe/abstract.cfm?URI=boe-6-2-574

[12] C. He, E. Yang, N. Patel, A. Ebrahimi, M. Shahbazi, P. Gehlbach, and I. Iordachita, "Automatic light pipe actuating system for bimanual robot-assisted retinal surgery," *IEEE/ASME Transactions on Mechatronics*, vol. 25, no. 6, pp. 2846–2857, 2020.

[13] H. Moon, D. Lee, and D. Nam, "Trimanual technique using assistant-controlled light probe illumination and wide-angle viewing system in 23-gauge sutureless vitrectomy for diabetic tractional retinal detachment," *Ophthalmic surgery, lasers & imaging retina*, vol. 46, pp. 73–6, 01 2015.

[14] T. C. Hutchens, A. Darafsheh, A. Fardad, A. N. Antoszyk, H. S. Ying, V. N. Astratov, and N. M. Fried, "Characterization of novel microsphere chain fiber optic tips for potential use in ophthalmic laser surgery," *Journal of Biomedical Optics*, vol. 17, no. 6, pp. 068 004–068 004, 2012.

[15] B. C. Becker, S. Yang, R. A. MacLachlan, and C. N. Riviere, "Towards vision-based control of a handheld micromanipulator for retinal cannulation in an eyeball phantom," in *2012 4th IEEE RAS & EMBS International Conference on Biomedical Robotics and Biomechatronics (BioRob)*, 2012, pp. 44–49.

[16] S. Yang, J. N. Martel, J. Louis A Lobes, and C. N. Riviere, "Techniques for robot-aided intraocular surgery using monocular vision," *The International Journal of Robotics Research*, vol. 37, no. 8, pp. 931–952, 2018. [Online]. Available: https://doi.org/10.1177/0278364918778352

[17] S. Yang, R. A. MacLachlan, J. N. Martel, L. A. Lobes, and C. N. Riviere, "Comparative evaluation of handheld robot-aided intraocular laser surgery," *IEEE Transactions on Robotics*, vol. 32, no. 1, pp. 246–251, 2016.

[18] Y. Koyama, M. M. Marinho, M. Mitsuishi, and K. Harada, "Autonomous coordinated control of the light guide for positioning in vitreoretinal surgery," *IEEE Transactions on Medical Robotics and Bionics*, vol. 4, no. 1, pp. 156–171, 2022.

[19] M. Mrochen and T. Seiler, "Influence of corneal curvature on calculation of ablation patterns used in photorefractive laser surgery," *Journal of Refractive Surgery*, vol. 17, no. 5, pp. 584–587, 2013.

[20] C. Niu, K. Li, D. Wang, W. Zhu, H. Xu, and J. Dong, "Gr-gan: A unified adversarial framework for single image glare removal and denoising," *Pattern Recognition*, vol. 156, p. 110815, 2024. [Online]. Available: https://www.sciencedirect.com/science/article/pii/S0031320324005661

[21] S. Ye, J.-L. Yin, B.-H. Chen, D. Chen, and Y. Wu, "Single image glare removal using deep convolutional networks," in *2020 IEEE International Conference on Image Processing (ICIP)*, 2020, pp. 201–205.

[22] M. Zhou, J. Wu, A. Ebrahimi, N. Patel, Y. Liu, N. Navab, P. Gehlbach, A. Knoll, M. A. Nasseri, and I. Iordachita, "Spotlight-based 3d instrument guidance for autonomous task in robot-assisted retinal surgery," *IEEE Robotics and Automation Letters*, vol. 6, no. 4, pp. 7750–7757, 2021.